An adaptive Ritz formulation for progressive damage modelling in variable angle tow composite plates

Dario Campagna [a], Vincenzo Oliveri [b], Ivano Benedetti [a,*]

[a] Department of Engineering, University of Palermo, Viale delle Scienze, Edificio 8, 90128, Palermo, Italy
[b] School of Engineering and Bernal Institute, University of Limerick, V94T9PX, Limerick, Ireland

ARTICLE INFO

ABSTRACT

In this work, an adaptive Ritz model for the analysis of variable angle tow composite plates featuring damage initiation and evolution under progressive loading is proposed, developed, implemented and tested. The plate kinematics is represented employing a first-order shear deformation theory, while the plate equilibrium equations at a given load step are obtained by minimizing the structure potential energy. The constitutive behaviour is modelled within the framework of continuum damage mechanics. In particular the initiation and evolution of damage, up to failure, are tracked by defining irreversible damage indices related to both fibres and matrix, both in tensile or compression loading. The discrete equations are then obtained by assuming a polynomial Ritz approximation of the primary kinematic variables in the energy minimization. Preliminary tests show how the application of the method as a single-domain approach induces the emergence of problematic spurious effects, related to Gibbs artefacts due to the inability of the selected polynomial basis to represent damage localization. An adaptive multi-domain technique is thus proposed to circumvent such issues, which has been successfully validated by benchmark tests. Eventually, original results about variable angle tow plates featuring damage evolution under progressive loading are presented.

1. Introduction

Multilayered composite materials enable the design of lightweight structures with improved stiffness, strength and fatigue properties when compared to metallic structures. For this reason, they find extensive applications in various fields of engineering, including the aerospace, naval, and automotive industries. Recent advancements in manufacturing techniques such as automated fibre placement, automated tape laying, and additive manufacturing have made it possible to create composite structures with variable mechanical properties [1–4]. This innovation has led to the development of Variable Angle Tow (VAT) laminates, in which the in-plane orientation of the fibres within the individual plies varies according to selected laws throughout the structure [5]. Significant advances have been made in the development and optimization of VAT composites, trying to identify the fibre patterns that may enhance properties of interest, e.g. the buckling load [6], the fundamental frequencies [7,8], or the dynamic response under low-speed impact [9].

Designers and engineers require modelling and computational tools capable of accurately predicting the structural response of the designed components. The need for such tools is particularly critical when new manufacturing techniques, as in the case of VAT composites, widen the design space. One of the most widely used computer methods for solving structural problems is the Finite Element Method (FEM) [10–13], which has also attained a recognized level of commercial maturity. Due to the high variability of the in-plane and through-the-thickness material features, the accurate FE analysis of VAT laminates critically depends on the quality and resolution of the employed mesh, thus generally attracting considerable computational costs [14]. To mitigate such problems and speed up the analysis, while retaining a high level of accuracy, various mesh-less methods have been developed as alternatives to FEM [15–18]. The Ritz method, which may be thought of as a global mesh-less technique in this context, has shown success in the study of conventional, laminated, and VAT composite structures [7,8, 19–22].

Although there is great interest in the study of VAT composites, not many works have focused on the study of damage evolution within them [23–25]. Modelling progressive damage in composite materials is challenging due to the many damage mechanisms that must be considered. Depending on the idealization scale, damage can be modelled in various ways, from the microscale to the macroscale. Using a micromechanical approach, damage initiation and evolution in heterogeneous materials can be investigated considering individual material

---

* Corresponding author.
  E-mail address: ivano.benedetti@unipa.it (I. Benedetti).

phases within representative volume elements (RVSs) [26–28]. Instead, at the macroscale laminate level, damage may be generally represented either as a softened region [29–31] or as a hard discontinuity [6,22]. At the intermediate mesoscale level, in which individual plies are represented as homogeneous, Continuum Damage Mechanics (CDM) is, among different approaches, one of the most employed frameworks for investigating the initiation and evolution of damage [32,33]. In CDM, damage is generally represented as a progressive loss of material stiffness and different FE approaches have been developed based on such modelling assumption [34–36].

Finite element formulations have also been employed to develop three dimensional CDM-based material models to simulate the progressive intra-laminar degradation of fibre reinforced laminates as well as delamination using cohesive interfaces between layers [37–39]. In addition to FE-based analysis methods, single domain meshless approaches, such as the Ritz method, have been shown to be effective, especially when dealing with smeared damaged zones [25].

However, in some cases, damage tends to concentrate in a narrow region due to specific loading conditions or initial imperfections [40, 41]. Within a classical single-domain Ritz approach, this localization of damage can introduce spurious effects when reconstructing the damaged state, commonly due to Gibbs effects, which can result in non-physical responses. Therefore, designers and engineers must be aware of the constraints and limitations associated with various modelling and computational tools when predicting the structural behaviour of composite materials and components.

Although the Ritz method offers several advantages, there is limited literature considering this approach to investigate damage initiation and evolution. Existing works on this topic often employ overly simplified damage models that provide a binary representation of damage [42], which are more suitable for identifying damage initiation rather than capturing damage evolution. Therefore, these approaches tend to be overly conservative.

The goal of this study is the development of a Ritz-based strategy able to consider the initiation and localization of damage, while providing physically objective responses. It will be shown as the employment of single-domain Ritz approximations in modelling damage gives rise to the mentioned spurious effects, that can be overcome by adopting an adaptive domain-splitting technique. The method still retains the advantages of the Ritz approach, ensuring reduced degrees of freedom compared to FE models while providing a highly accurate description of the damage process and a physically meaningful response. The modelling of damage initiation and evolution through the proposed hp-adaptive multi-domain Ritz method constitutes the key novelty of the present contribution.

The manuscript is structured as follows: Section 2 specifies the considered problem, introduces the geometric description of the plate, the kinematic model, the constitutive relations employed to take into account the presence of damage and the plate governing equations derived using the principle of minimum potential energy. In Section 3, using the Ritz solution scheme, the discrete form of governing equations is built and written in incremental form to solve the non-linear damage evolution problem. Moreover, some details about the implementation into numerical software are given. In Section 4 firstly, some results about spurious numerical effects that may arise using single-domain discretizations are presented, and then results concerning the multi-domain adaptive strategy adopted in this work are shown. Finally, after the validation of the proposed approach, results of different VAT composite plates are presented. Section 5 discusses the strengths and limitations of the present work before Conclusions are drawn.

2. Plate modelling

In this section, the key items of the formulation are briefly presented and discussed.
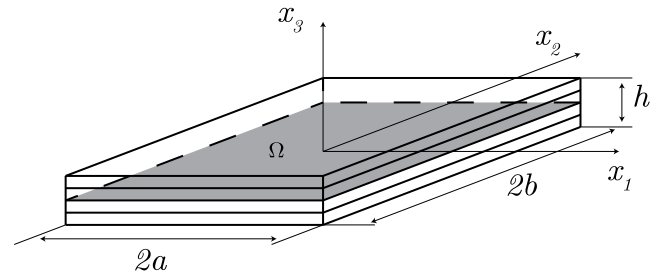

Fig. 1. Schematic representation of multilayered composite plate.
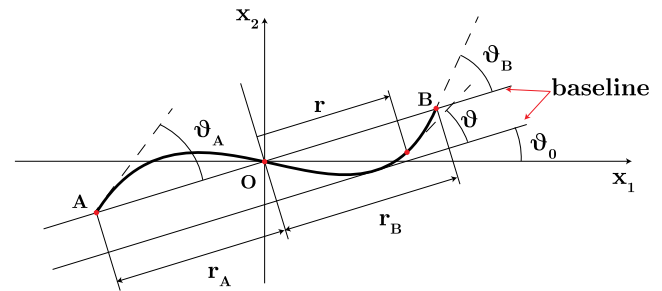

Fig. 2. Geometric description of VAT lamina for fibre orientation definition.

2.1. Problem statement

A quadrilateral laminated composite plate referred to a Cartesian coordinate system x_1, x_2, x_3, with the axis x_3 directed along the thickness h, is considered, as shown in Fig. 1. The reference mid-plane lies on the plane $x_1 x_2$ and is denoted by Ω while $\delta\Omega$ identifies its boundary.

The plate is assembled from N_{ply} VAT laminae, whose reinforcing fibres follow curved paths, thus exhibiting varying angles concerning the structural reference directions. Such fibre paths are described by specifying suitable laws for the fibre orientation θ. In this study, referring to Fig. 2, the following law is used

$$\theta = \theta_0 + \frac{\theta_A r_B - \theta_B r_A}{r_B - r_A} + |r| \frac{\theta_B - \theta_A}{r_B - r_A} \qquad (1)$$

where θ_0 is the angle between the baseline and the axis x_1, θ_A and θ_B measure the angle of the fibres at the points A and B, whilst r_A and r_B are the distances of these points from the projection O' of the plate centre on the baseline. Following the notation introduced by Gurdal et al. [5], point A is assumed to coincide with the projection of the centre point of the plate O' and $r_B = 2a$, so that the law that describes the fibre path of a lamina can be denoted as $\theta_0 + \langle \theta_A | \theta_B \rangle$.

To model general quadrilateral plates, a natural coordinate system $(\xi, \eta) \in [-1, 1] \times [-1, 1]$ is introduced, as in Fig. 3. The in-plane coordinates are given by

$$x_i = \sum_{\alpha=1}^{4} g_\alpha(\xi, \eta) x_{i\alpha}, \qquad i = 1, 2 \qquad (2)$$

where $x_{i\alpha}$ are the coordinates of the αth vertex of the plate mid-plane and g_α are the standard bi-linear shape functions, namely,

$$g_\alpha = \frac{(-1)^{\alpha-1}}{4}(\xi + \xi_\alpha)(\eta + \eta_\alpha), \qquad \alpha = 1, \dots, 4 \qquad (3)$$

2.2. Kinematic assumptions

In the present formulation, the plate kinematics is based on the *First-order shear deformation theory* (FSDT) [43]. Thus, the displacement vector components $\boldsymbol{d} = \{d_1, d_2, d_3\}^\intercal$ are given by
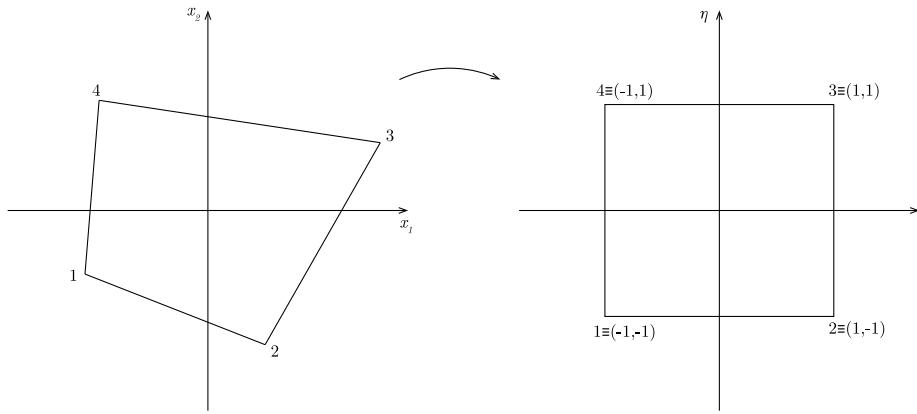
Fig. 3. Plate mid-plane mapping: from the general quadrilateral domain in the $x_1 x_2$ coordinate system to square domain $[-1;1] \times [-1;1]$ in $\xi\eta$ natural coordinate system.

$$d_1 = u_1(x_1, x_2) + x_3 \vartheta_1(x_1, x_2) \tag{4a}$$

$$d_2 = u_2(x_1, x_2) + x_3 \vartheta_2(x_1, x_2) \tag{4b}$$

$$d_3 = u_3(x_1, x_2) \tag{4c}$$

where u_1 and u_2 are the mid-plane in-plane displacement components, u_3 is the mid-plane transverse deflection, ϑ_1 and ϑ_2 are the section rotations. Eq. (4) can be compactly written as,

$$d = u + x_3 L \vartheta \tag{5}$$

where, $u = \{u_1, u_2, u_3\}^\mathsf{T}$, $\vartheta = \{\vartheta_1, \vartheta_2, \vartheta_3\}^\mathsf{T}$ and

$$L = \begin{bmatrix} 1 & 0 & 0 \\ 0 & 1 & 0 \\ 0 & 0 & 0 \end{bmatrix}. \tag{6}$$

It is worth noting that ϑ_3 is a "drilling" rotation that does not affect the plate deformation and it is used only to enforce the multi-domain interface continuity condition as described in Section 3.2.1.

The strain vector e is partitioned into in-plane and out-of-plane components, denoted by the subscripts p and n respectively,

$$e = \{e_{11}, e_{22}, e_{12}, e_{13}, e_{23}, e_{33}\}^\mathsf{T} = \begin{Bmatrix} e_p \\ e_n \end{Bmatrix}, \tag{7}$$

with

$$e_p = \mathcal{D}_p u + x_3 \mathcal{D}_p L \vartheta = \varepsilon + x_3 \kappa \tag{8a}$$

$$e_n = \mathcal{D}_n u + L \vartheta = \gamma \tag{8b}$$

where ε, κ and γ denote the in-plane strains, curvatures and shear strains vectors, respectively, and $\mathcal{D}_p$ and $\mathcal{D}_n$ are matrix linear differential operators whose explicit expression is given in Appendix A.

2.3. Constitutive description in the presence of damage

In this section, the constitutive relations for a VAT lamina are presented considering the possible presence of damage.

For the kth pristine lamina, assuming plane stress conditions, the relations

$$\sigma_p = Q_p(\theta) e_p, \qquad \sigma_n = Q_n(\theta) e_n \tag{9}$$

hold, which link the components of stress and strain in the plate structural reference system x_1, x_2, x_3 through the coefficient matrices $Q_p(\theta)$ and $Q_n(\theta)$. In general, the coefficient matrices, whose explicit expression is given in Appendix B, depend on the local fibre orientation θ that, in VAT composites, vary over the lamina itself [44].

Following a classical CDM approach, the presence of damage can be considered by expressing the link between in-plane components of stress and strain within a lamina as

$$\sigma_p = \hat{Q}_p(\theta, \omega) e_p, \tag{10}$$

where $\omega = \{\omega_1, \omega_2, \omega_6\}^\mathsf{T}$ is a vector collecting the damage indices associated with the considered point in the lamina, which express the level of longitudinal, transverse and shear material degradation respectively. More explicitly

$$\hat{Q}_p(\theta, \omega) = T(\theta) \overline{Q}_p(\omega) \tag{11}$$

where $T(\theta)$ is the transformation matrix linking the structural and material reference system and

$$\overline{Q}_p = \frac{1}{D} \begin{bmatrix} (1-\omega_1)E_1 & (1-\omega_1)(1-\omega_2)\nu_{12}E_1 & 0 \\ (1-\omega_1)(1-\omega_2)\nu_{12}E_2 & (1-\omega_2)E_2 & 0 \\ 0 & 0 & D(1-\omega_6)G_{12} \end{bmatrix}, \tag{12}$$

is the matrix linking the components of stress and strains in the material reference system, aligned with the local fibre direction. In Eq. (12) E_i are the Young's moduli, G_{ij} are the shear moduli, ν_{ij} are the Poisson's coefficients and

$$D = 1 - (1-\omega_1)(1-\omega_2)\nu_{12}\nu_{21}. \tag{13}$$

Each damage index ω_i varies between 0, when no damage is present, and 1, which indicates material failure.

Damage is activated when the local in-plain stress components fulfil certain threshold conditions, which, in this work, are specified following the Hashin's criteria [45,46]. In particular, four different activation conditions are considered, differentiating the case of tensile or compression fibre damage activation

$$Fibre \begin{cases} \left(\frac{\sigma_{11}}{X_T}\right)^2 = 1 & Tension \\ \left(\frac{\sigma_{11}}{X_C}\right)^2 = 1 & Compression \end{cases} \tag{14}$$

from the case of matrix damage activation

$$Matrix \begin{cases} \left(\frac{\sigma_{22}}{Y_T}\right)^2 + \left(\frac{\sigma_{12}}{S_L}\right)^2 = 1 & Tension \\ \left(\frac{\sigma_{22}}{2S_T}\right)^2 + \left[\left(\frac{Y_C}{2S_T}\right)^2 - 1\right]\frac{\sigma_{22}}{Y_C} + \left(\frac{\sigma_{12}}{S_L}\right)^2 = 1 & Compression. \end{cases} \tag{15}$$

In the above equations X_T and X_C are the strengths in the fibre direction either in tension or compression, Y_T and Y_C denote the tensile and compression strengths in matrix direction, while S_T and S_L are the longitudinal and transverse shear strengths.

Once damage is activated, further increases in the effective loads generally result in the evolution of the activated damage indices and
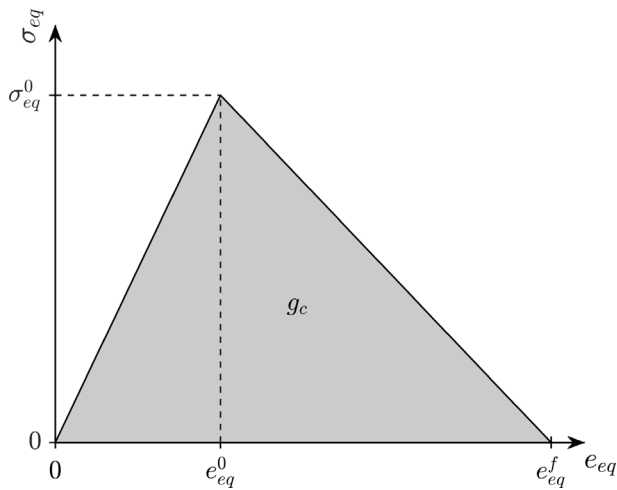
Fig. 4. Strain-softening constitutive behaviour.

thus in the degradation of the material properties associated with them. The strain-softening constitutive behaviour adopted in this work is linear, as shown in Fig. 4. The evolution of each damage variable is assessed through equivalent strains that, for each loading/damage mode, are given by

$$Fibres \begin{cases} e_{ft,eq} = \langle e_{11} \rangle \\ e_{fc,eq} = \langle -e_{11} \rangle \end{cases} \quad Matrix \begin{cases} e_{mt,eq} = \sqrt{\langle e_{22} \rangle^2 + e_{12}^2} \\ e_{mc,eq} = \sqrt{\langle -e_{22} \rangle^2 + e_{12}^2} \end{cases}$$

(16)

where $\langle \circ \rangle = (\circ + |\circ|)/2$ denotes the Macaulay brackets and the subscripts ft, fc, mt, mc refer to fibres in tension and compression and matrix in tension and compression respectively.

During the loading process, the value of the ith damage index can be computed as

$$\omega_i(\tau) = \frac{e_{i,eq}^f \left(e_{i,eq} - e_{i,eq}^0 \right)}{e_{i,eq} \left(e_{i,eq}^f - e_{i,eq}^0 \right)}, \qquad i = ft, fc, mt, mc,$$

(17)

where τ denotes a generic loading/time ordering parameter spanning the loading history $\mathcal{H}$, $e_{i,eq}^0$ is the equivalent strain at the onset of damage and $e_{i,eq}^f$ is the equivalent strain at rupture ($\omega_i = 1$). Moreover, to ensure a monotonically increasing evolution, the current value of the ith damage index is defined as

$$\omega_i = \max\{0, \min\{\max_{\tau \in \mathcal{H}}\{\omega_i(\tau)\}, 1\}\}.$$

(18)

It is worth noting that, in general, different values of damage are associated with tensile or compression loading, which means that, for example, two different values of ω_1 are defined with respect to the fibres direction at a given material point, and Eq. (18) must be updated distinguishing tensile form compression loading, see e.g. Ref. [36].

In Eq. (17), the strain at rupture $e_{i,eq}^f$ can be computed from the knowledge of the material fracture toughness G_c [47,48]. To ensure that the fracture toughness remains constant, $e_{i,eq}^f$ must be adjusted introducing a discretization dependent length L_c, which modifies the shape of the strain-softening curve linking it to the size of the discretization itself, see e.g. Refs. [49,50]. In Fig. 4, the area under the stress–strain curve

$$g_c = \int_0^{e_{eq}^f} \sigma_{eq} \, de_{eq}$$

(19)

corresponds to the energy dissipated at failure per unit volume. Defining the *equivalent displacement* as $\delta_{eq} = e_{eq}L_c$, the fracture energy

dissipated per unit area can be written as

$$G_c = g_c L_c = \int_0^{\delta_{eq}^f} \sigma_{eq} \, d\delta_{eq}.$$

(20)

Considering that the fracture energy G_c is a known material property, $e_{i,eq}^f$ can be eventually computed as

$$e_{i,eq}^f = \frac{2G_c}{\sigma_{eq}^0 L_c}.$$

(21)

While in finite element models L_c is directly linked to the mesh size, in the proposed Ritz scheme

$$L_c = \sqrt{\frac{S}{M_\chi N_\chi}}$$

(22)

where S is the area of the discretized domain, whilst M_χ and N_χ are the maximum degrees of the polynomial Ritz approximation scheme, which will be further discussed in the subsequent section.

2.4. Variational statement and governing equations

The plate equilibrium equations are obtained by minimizing the variation of the potential energy, considering the plate kinematic assumptions and the constitutive equations.

The stationarity of the total potential energy at a given load level reads

$$\delta\Pi = \delta U + \delta V = 0,$$

(23)

where U is the structure internal energy and V is the work done by the external forces. Considering the plate kinematics and constitutive relations given in Sections 2.2 and 2.3, the internal energy U may be written as

$$U = \frac{1}{2} \int_\Omega \sum_{k=1}^{N_{ply}} \left\{ \int_{h_{k-1}}^{h_k} \left(e_p^\mathsf{T}\sigma_p + e_n^\mathsf{T}\sigma_n \right) dx_3 \right\} d\Omega =$$
$$= \frac{1}{2} \int_\Omega \sum_{k=1}^{N_{ply}} \left\{ \int_{h_{k-1}}^{h_k} \left[\left(\varepsilon^\mathsf{T} + x_3\kappa^\mathsf{T} \right) Q_p^{\langle k \rangle} \left(\varepsilon + x_3\kappa \right) + \gamma^\mathsf{T} Q_n^{\langle k \rangle} \gamma \right] dx_3 \right\} d\Omega$$

(24)

while the external work is given by

$$V = -\int_\Omega \left(u^\mathsf{T}q + \vartheta^\mathsf{T}m \right) d\Omega - \int_{\partial\Omega} \left(u^\mathsf{T}\overline{N} + \vartheta^\mathsf{T}\overline{M} \right) d\partial\Omega$$

(25)

where $q = \{q_1, q_2, q_3\}^\mathsf{T}$ and $m = \{m_1, m_2, 0\}^\mathsf{T}$ are the external forces and moments per unit area applied over the domain Ω, whereas $\overline{N}$ and $\overline{M}$ denote prescribed forces and moments applied along the plate boundary $\partial\Omega_l \subset \partial\Omega$. The plate essential boundary conditions are provided by prescribing the generalized displacements on the boundary $\partial\Omega_c$ as follows

$$\Xi_u u = \Xi_u \bar{u} \quad \text{on } \partial\Omega_c$$
$$\Xi_\vartheta \vartheta = \Xi_\vartheta \bar{\vartheta} \quad \text{on } \partial\Omega_c$$

(26)

where Ξ_u and Ξ_ϑ are Boolean matrix operators used for selecting the desired constrained generalized displacements, whereas the over-bar denotes prescribed quantities.

3. Ritz solution scheme

Once the plate governing equations – Eqs. (23)–(24)–(25) – have been written, their discrete form can be built using the Ritz approximation scheme developed e.g. in Refs. [19,20]. The main items of the solution procedure are outlined in this section.

3.1. Ritz polynomial approximation

The Ritz scheme expresses the components of the generalized displacements appearing in Eqs. (23)–(24) as

$$\chi = \sum_{m=1}^{M_\chi} \sum_{n=1}^{N_\chi} \psi_m(\xi)\, \psi_n(\eta)\, C_{\chi_{(m-1)M+n}} = \boldsymbol{\Psi}_\chi \boldsymbol{C}_\chi \tag{27}$$

where $\chi \in \{u_1, u_2, u_3, \vartheta_1, \vartheta_2\}$ is the generic component of displacement, $\psi_m(\xi)$ and $\psi_n(\eta)$ are the trial function of order m or n and $C_{\chi_{(m-1)M+n}}$ are the unknown Ritz coefficients. In this work, among other possible choices, Legendre orthogonal polynomials

$$\psi_n(\zeta) = \frac{1}{2^n n!} \frac{d^n}{d\zeta^n}\left[\left(\zeta^2 - 1\right)^n\right], \tag{28}$$

have been selected as trial functions $\psi_m(\xi)$ and $\psi_n(\eta)$, as they proved effective in plate problems [51].

Eq. (27) can be specialized to the plate primary variables $\boldsymbol{u}$ and $\boldsymbol{\vartheta}$ and written in compact matrix form as

$$\boldsymbol{u} = \begin{bmatrix} \boldsymbol{\Psi}_{u_1} & 0 & 0 \\ 0 & \boldsymbol{\Psi}_{u_2} & 0 \\ 0 & 0 & \boldsymbol{\Psi}_{u_3} \end{bmatrix} \begin{Bmatrix} \boldsymbol{C}_{u_1} \\ \boldsymbol{C}_{u_2} \\ \boldsymbol{C}_{u_3} \end{Bmatrix} = \begin{bmatrix} \boldsymbol{\Phi}_{u_1} \\ \boldsymbol{\Phi}_{u_2} \\ \boldsymbol{\Phi}_{u_3} \end{bmatrix} \boldsymbol{U} = \boldsymbol{\Phi}_u \boldsymbol{U} \tag{29}$$

and

$$\boldsymbol{\vartheta} = \begin{bmatrix} \boldsymbol{\Psi}_{\vartheta_1} & 0 & 0 \\ 0 & \boldsymbol{\Psi}_{\vartheta_2} & 0 \\ 0 & 0 & \boldsymbol{\Psi}_{\vartheta_3} \end{bmatrix} \begin{Bmatrix} \boldsymbol{C}_{\vartheta_1} \\ \boldsymbol{C}_{\vartheta_2} \\ \boldsymbol{C}_{\vartheta_3} \end{Bmatrix} = \begin{bmatrix} \boldsymbol{\Phi}_{\vartheta_1} \\ \boldsymbol{\Phi}_{\vartheta_2} \\ \boldsymbol{\Phi}_{\vartheta_3} \end{bmatrix} \boldsymbol{\Theta} = \boldsymbol{\Phi}_\vartheta \boldsymbol{\Theta}. \tag{30}$$

Using the above equations, the in-plane strain vector $\boldsymbol{\varepsilon}$, the curvatures vector $\boldsymbol{\kappa}$ and the shear strains vector $\boldsymbol{\gamma}$ can be written as

$$\boldsymbol{\varepsilon} = \mathcal{B}_{pU} \boldsymbol{U}$$
$$\boldsymbol{\kappa} = \mathcal{B}_{p\Theta} \boldsymbol{\Theta}, \qquad \boldsymbol{\gamma} = \mathcal{B}_{nU} \boldsymbol{U} + \mathcal{B}_{i\Theta} \boldsymbol{\Theta} \tag{31}$$

where the operators $\mathcal{B}$ are given by

$$\begin{aligned} \mathcal{B}_{pU} &= \boldsymbol{D}_p \boldsymbol{\Phi}_u & \mathcal{B}_{p\Theta} &= \boldsymbol{D}_p \boldsymbol{\Phi}_\vartheta \\ \mathcal{B}_{nU} &= \boldsymbol{D}_n \boldsymbol{\Phi}_u & \mathcal{B}_{i\Theta} &= \boldsymbol{\Phi}_\vartheta \end{aligned} \tag{32}$$

3.2. Ritz discrete solving system

By considering Eqs. (29)–(30) and employing a penalty approach to enforce the essential boundary conditions, the stationarity condition $\delta\Pi = 0$ with respect to $\boldsymbol{U}$ and $\boldsymbol{\Theta}$ leads to the discrete system

$$\begin{aligned} &\int_\Omega \left[\mathcal{B}_{pU}^\mathsf{T} \boldsymbol{A} \mathcal{B}_{pU} + \mathcal{B}_{nU}^\mathsf{T} \boldsymbol{A}_s \mathcal{B}_{nU} \right] \boldsymbol{U}\, d\Omega + \int_\Omega \Big[\mathcal{B}_{pU}^\mathsf{T} \boldsymbol{B} \mathcal{B}_{p\Theta} \\ &\qquad\qquad + \mathcal{B}_{nU}^\mathsf{T} \boldsymbol{A}_s \mathcal{B}_{i\Theta} \Big] \boldsymbol{\Theta}\, d\Omega \\ &+ \int_\Omega \left[\mathcal{B}_{p\Theta}^\mathsf{T} \boldsymbol{B} \mathcal{B}_{pU} + \mathcal{B}_{i\Theta}^\mathsf{T} \boldsymbol{A}_s \mathcal{B}_{nU} \right] \boldsymbol{U}\, d\Omega + \int_\Omega \Big(\mathcal{B}_{p\Theta}^\mathsf{T} \boldsymbol{D} \mathcal{B}_{p\Theta} \\ &\qquad\qquad + \mathcal{B}_{i\Theta}^\mathsf{T} \boldsymbol{A}_s \mathcal{B}_{i\Theta} \Big) \boldsymbol{\Theta}\, d\Omega \\ &+ \int_{\partial\Omega_c} \left(\boldsymbol{\Phi}_u^\mathsf{T} \boldsymbol{\Xi}_u^\mathsf{T} \boldsymbol{\mu}_u \boldsymbol{\Xi}_u \boldsymbol{\Phi}_u \boldsymbol{U} + \boldsymbol{\Phi}_\vartheta^\mathsf{T} \boldsymbol{\Xi}_\vartheta^\mathsf{T} \boldsymbol{\mu}_\vartheta \boldsymbol{\Xi}_\vartheta \boldsymbol{\Phi}_\vartheta \boldsymbol{\Theta} \right) d\partial\Omega \\ &= \int_\Omega \left(\boldsymbol{\Phi}_u^\mathsf{T} \boldsymbol{q} + \boldsymbol{\Phi}_\vartheta^\mathsf{T} \boldsymbol{m} \right) d\Omega + \int_{\partial\Omega_l} \left(\boldsymbol{\Phi}_u^\mathsf{T} \overline{\boldsymbol{N}} + \boldsymbol{\Phi}_\vartheta^\mathsf{T} \overline{\boldsymbol{M}} \right) d\partial\Omega \\ &+ \int_{\partial\Omega_c} \left(\boldsymbol{\Phi}_u^\mathsf{T} \boldsymbol{\Xi}_u^\mathsf{T} \boldsymbol{\mu}_u \boldsymbol{\Xi}_u \boldsymbol{\Phi}_u\, \bar{\boldsymbol{u}} + \boldsymbol{\Phi}_\vartheta^\mathsf{T} \boldsymbol{\Xi}_\vartheta^\mathsf{T} \boldsymbol{\mu}_\vartheta \boldsymbol{\Xi}_\vartheta \boldsymbol{\Phi}_\vartheta\, \bar{\boldsymbol{\vartheta}} \right) d\partial\Omega, \end{aligned} \tag{33}$$

where $\boldsymbol{A}$, $\boldsymbol{B}$, $\boldsymbol{D}$ and $\boldsymbol{A}_s$ represent the plate generalized stiffness matrices given by

$$\begin{aligned} \boldsymbol{A} &= \sum_{k=1}^{N_{ply}} \int_{h_{k-1}}^{h_k} \hat{\boldsymbol{Q}}_p^{\langle k \rangle}(\theta, \omega)\, dx_3 & \boldsymbol{B} &= \sum_{k=1}^{N_{ply}} \int_{h_{k-1}}^{h_k} x_3 \hat{\boldsymbol{Q}}_p^{\langle k \rangle}(\theta, \omega)\, dx_3 \\ \boldsymbol{D} &= \sum_{k=1}^{N_{ply}} \int_{h_{k-1}}^{h_k} x_3^2 \hat{\boldsymbol{Q}}_p^{\langle k \rangle}(\theta, \omega)\, dx_3 & \boldsymbol{A}_s &= \sum_{k=1}^{N_{ply}} \int_{h_{k-1}}^{h_k} \boldsymbol{Q}_n^{\langle k \rangle}(\theta)\, dx_3, \end{aligned} \tag{34}$$

where the summation is made for each *k*th ply in the laminate, while $\boldsymbol{\mu}_u$ and $\boldsymbol{\mu}_\vartheta$ are diagonal matrices containing the penalty coefficients. Eq. (33) may conveniently written in compact form as

$$\left(\boldsymbol{K}_0 + \boldsymbol{R} \right) \boldsymbol{X} = \boldsymbol{F}_D + \boldsymbol{F}_L \tag{35}$$

where $\boldsymbol{X} = \{\boldsymbol{U}, \boldsymbol{\Theta}\}^\mathsf{T}$ is the vector collecting the unknown coefficients of the Ritz series expansion, $\boldsymbol{K}_0$ is the stiffness matrix, and $\boldsymbol{R}$ is the matrix originating from the enforcement of the BCs through a penalty approach. On the right-hand side, the vectors $\boldsymbol{F}_D$ and $\boldsymbol{F}_L$ collect the discrete terms associated with the external loads. Details on the matrices appearing in Eq. (35) are given in Appendix C.

To solve the non-linear problem given in Eq. (35), an incremental-iterative procedure is employed. It is important to observe that the local stiffness of the laminate layers, and thus the stiffness matrix $\boldsymbol{K}_0$, is affected by the damage level $\boldsymbol{\omega}[\mathcal{H}(\boldsymbol{X})]$. The vector $\boldsymbol{\omega}[\mathcal{H}(\boldsymbol{X})]$, which collects the damage indices, plays the role of an internal state vector that depends on the loading/solution history $\mathcal{H}(\boldsymbol{X})$. Noting this, the incremental form of Eq. (35) may be expressed as

$$\boldsymbol{R}\, \Delta\boldsymbol{X} + \Delta\left[\boldsymbol{K}_0 \boldsymbol{X}\right] = \Delta\boldsymbol{F}_D + \Delta\boldsymbol{F}_L \tag{36}$$

with

$$\Delta\left[\boldsymbol{K}_0 \boldsymbol{X}\right] = \boldsymbol{K}_{t,dmg}\, \Delta\boldsymbol{X}, \tag{37}$$

where $\Delta(\circ)$ is the incremental operator, whilst $\boldsymbol{K}_{t,dmg}$ is the tangent stiffness matrix contribution related to the damage evolution. Further details are reported in Appendix D.

3.2.1. Multidomain Ritz model: sub-domains continuity conditions

As mentioned in the *Introduction*, the direct application of a Ritz approximation to problems involving a hard discontinuity, e.g. a damage localization or crack, gives rise to artefacts induced by the unavoidable presence of Gibbs effects. This issue, which will be further highlighted and investigated in the numerical tests, has called for the development of mitigation strategies able to ensure the objectivity of the response upon damage localization. Among various strategies, an adaptive subdivision of the Ritz analysis domain into smaller subdomains, over which hierarchical variable order Ritz approximations are further adopted, has proved one of the most promising in contrasting the observed issue. The subdivision scheme is here described, together with the method used to transfer the information from a parent domain to its children ones, and it will be further discussed in the subsequent sections.

Consider the original plate subdivided into N_{el} quadrilateral sub-domains; the quantities associated with such sub-domains are denoted by the superscript $\langle t \rangle$. Each separate sub-domain $\langle t \rangle$ is mapped into its corresponding natural coordinate system and is associated with its governing equations provided in Eq. (35). Let Γ_{pq} denote the edge shared between two contiguous sub-domains $\langle p \rangle$ and $\langle q \rangle$: the integrity of the domain requires displacement continuity and traction equilibrium along Γ_{pq}.

The displacement continuity on Γ_{pq} requires that: (*i*) the modelling plane translations of the two contiguous sub-domains have equal components in the global reference system $x_1 x_2 x_3$; (*ii*) the rotations around the global axes x_i of the two contiguous sub-domains are equal. These considerations give

$$\boldsymbol{\Lambda}_u^{\langle p \rangle} \boldsymbol{u}^{\langle p \rangle} = \boldsymbol{\Lambda}_u^{\langle q \rangle} \boldsymbol{u}^{\langle q \rangle} \qquad \text{on } \Gamma_{pq} \tag{38a}$$

$$\boldsymbol{\Lambda}_\vartheta^{\langle p \rangle} \boldsymbol{\vartheta}^{\langle p \rangle} = \boldsymbol{\Lambda}_\vartheta^{\langle q \rangle} \boldsymbol{\vartheta}^{\langle q \rangle} \qquad \text{on } \Gamma_{pq} \tag{38b}$$

where $\boldsymbol{\Lambda}_\alpha^{\langle r \rangle}$ are suitable transformation matrices from the local to the global reference systems. It is worth noting that the introduction of the drilling rotation θ_3 does not affect the plate displacements but it allows to generalize the rotation continuity condition through Eq. (38b), see e.g. Ref. [52].

On the other hand, the traction equilibrium is enforced in terms of resultant forces and moments along Γ_{pq}, written as

$$\boldsymbol{\Lambda}_u^{\langle p \rangle} \tilde{\boldsymbol{N}}^{\langle p \rangle} + \boldsymbol{\Lambda}_u^{\langle q \rangle} \tilde{\boldsymbol{N}}^{\langle q \rangle} = \boldsymbol{0} \tag{39a}$$

$$\boldsymbol{\Lambda}_\vartheta^{\langle p \rangle} \tilde{\boldsymbol{M}}^{\langle p \rangle} + \boldsymbol{\Lambda}_\vartheta^{\langle q \rangle} \tilde{\boldsymbol{M}}^{\langle q \rangle} = \boldsymbol{0} \tag{39b}$$
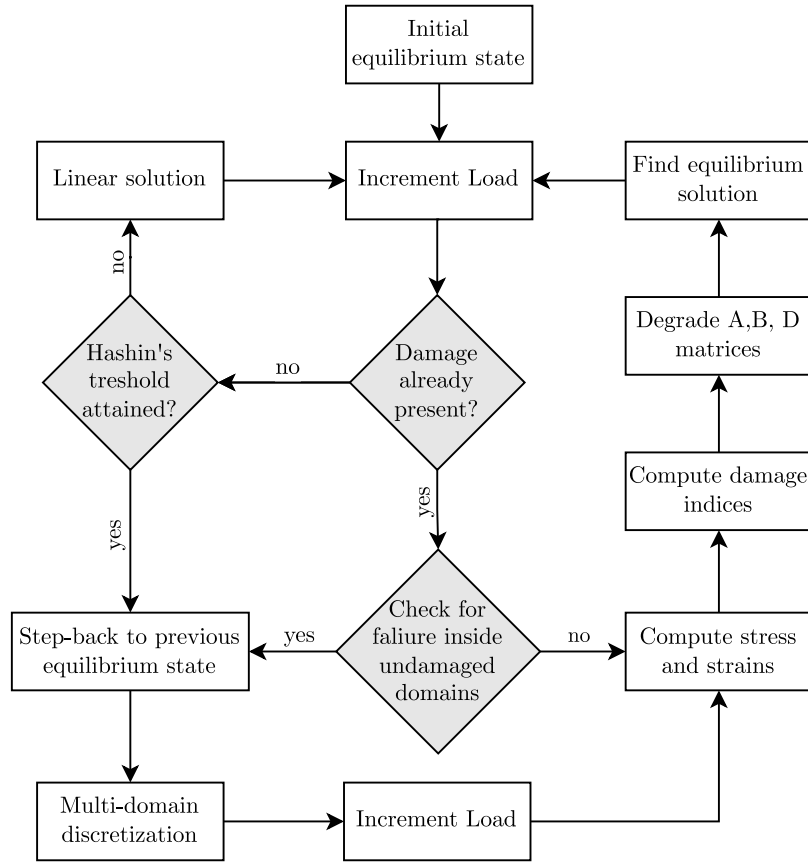
Fig. 5. Block diagram representing the phases of the adaptive Ritz damage model.

The overall set of discrete equations, considering the subdivision of the original domain into sub-domains, is then obtained by applying the variational formulation and Ritz approximation scheme to all the sub-domains, and enforcing the boundary and continuity conditions expressed in Eq. (38) through suitable penalty terms, see e.g. Ref. [53]. Therefore, the resolving system of equations, for $t = 1 \ldots N_{el}$ is

$$\left(\boldsymbol{K}_0^{\langle t \rangle} + \boldsymbol{R}^{\langle t \rangle} + \sum_{\substack{r=1 \\ r \neq t}}^{N_{el}} \boldsymbol{P}_{rt}^{\langle t,t \rangle} \right) \boldsymbol{X}^{\langle t \rangle} - \sum_{\substack{r=1 \\ r \neq t}}^{N_{el}} \boldsymbol{P}_{rt}^{\langle t,r \rangle} \boldsymbol{X}^{\langle r \rangle} = \boldsymbol{F}_D^{\langle t \rangle} + \boldsymbol{F}_L^{\langle t \rangle}, \qquad (40)$$

where the matrices $\boldsymbol{P}_{rt}^{\langle \cdots \rangle}$, explicitly given in Appendix C, are introduced to properly describe the connection between sub-domains.

The incremental form associated with Eq. (40) is eventually given by

$$\left[\boldsymbol{R}^{\langle t \rangle} + \sum_{\substack{r=1 \\ r \neq t}}^{N_{el}} \boldsymbol{P}_{rt}^{\langle t,t \rangle} \right] \Delta \boldsymbol{X}^{\langle t \rangle} - \left[\sum_{\substack{r=1 \\ r \neq t}}^{N_{el}} \boldsymbol{P}_{rt}^{\langle t,r \rangle} \right] \Delta \boldsymbol{X}^{\langle r \rangle} + \Delta \left[\boldsymbol{K}_0^{\langle t \rangle} \boldsymbol{X}^{\langle t \rangle} \right] = \Delta \boldsymbol{F}_D^{\langle t \rangle} + \Delta \boldsymbol{F}_L^{\langle t \rangle}$$

$$(41)$$

for $t = 1 \ldots N_{el}$.

3.3. Implementation details

The proposed model has been implemented using MATLAB® [54].

In this study, the nonlinear damage evolution problem is solved by employing an incremental-iterative Newton–Raphson scheme in displacement control. Once the solution at a given load step is obtained, a load increment is enforced, and the Newton–Raphson iteration is started, triggering the non-linear evolution of the internal damage

variables; the process is arrested when the residual is reduced below a preset tolerance, so that a subsequent increment, if of interest, may be applied. A block diagram describing the most relevant phases of the implemented model is reported in Fig. 5.

Some remarks about how the adaptive multi-domain procedure works are herein reported. All the subdomains are initially flagged as *undamaged*, unless some *a priori* damage is considered. If, upon load increment, the failure criteria are met in an undamaged sub-domain, then the adaptive procedure is activated. Hence, the program steps back to the previous converged solution and subdivides the considered sub-domain, which is going to feature damage initiation, into a collection of patches. It is worth mentioning an important constrain that must be considered in the subdivision process: the stress–strain diagram must not present snap-back that may arise after the computation of $e_{i,eq}^f$ in Eq. (21). To ensure that, the maximum size for the new sub-domains in which damage can spread is:

$$L_c \leq \frac{2 E_i G_{c,i}}{X_i} \qquad i = ft, fc, mt, mc, \qquad (42)$$

where E_i, $G_{c,i}$ and X_i are the Young modulus, fracture energies and strengths associated with their corresponding damage modes, respectively. This is consistent with what often done in CDM approaches, see e.g. [47,55]. Those new sub-domains are still flagged as undamaged, except those within which the damage threshold will be overcome by re-applying the load increment.

To transfer the fields information from the last converged state, involving a certain set of domains, to the new subdivided domains, a least square procedure is employed. Therefore, after computing and assembling the stiffness and penalty matrices, the solution vector of the new discretization X_m is computed by equating the displacement field of the previous discretization and the multi-domain discretization of
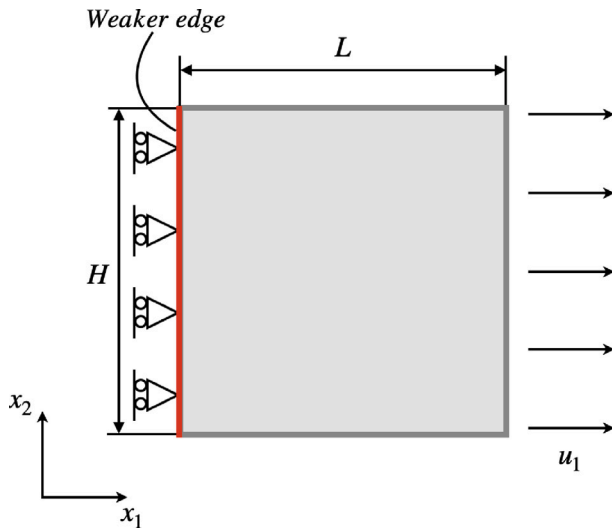
Fig. 6. Schematic representation of square plate loaded with a prescribed displacement u_1 in the x_1 direction applied on the right edge.

Table 1
Material properties of straight fibre lamina.

Properties	Values
Modulus [GPa]	$E_{11} = 105.0$; $E_{22} = 8.57$; $G_{23} = G_{13} = 3.05$; $G_{12} = 4.39$
Poisson's ratio	$v_{12} = 0.34$
Strength [MPa]	$X^T = 1400.0$; $X^C = 930.0$; $Y^T = 47.0$; $Y^C = 60.3$; $S^L = S^T = 53.0$
Fracture toughness [kJ m^{-2}]	$G_{c,ft} = 200$; $G_{c,fc} = 100$ $G_{c,mt} = 1.0$; $G_{c,mc} = 1.0$

the available converged solution,

$$u(x_1, x_2) = \tilde{u}(x_1, x_2) = \boldsymbol{\Phi}(x_1, x_2)X = \tilde{\boldsymbol{\Phi}}(x_1, x_2)X_m \quad (43)$$

where $\tilde{u}$ and $\tilde{\boldsymbol{\Phi}}(x_1, x_2)$ are respectively the displacements and the matrix of polynomials associated with the new discretization. The solution vector X_m is then obtained by minimizing not only $\|\tilde{\boldsymbol{\Phi}}(x_1, x_2)X_m - \boldsymbol{\Phi}(x_1, x_2)X\|$ but also $\|X_m\|$ [56].

Finally, it is worth highlighting an important implementation feature before presenting the validation and numerical result; convergence issues are frequent and well-known in material models that show softening and stiffness loss. In this study, a viscous regularization approach is used as mentioned in Ref. [34], to mitigate such numerical convergence issues. The following evolution equation is then introduced

$$\dot{\omega}_i^v = \frac{1}{\beta}\left(\omega_i - \omega_i^v\right) \quad (44)$$

where β is a *viscous parameter* and ω_i^v denotes the regularized damaged variable for the ith damage mode, computed as

$$\omega_i^v|_n = \frac{\Delta\tau}{\beta + \Delta\tau}\omega_i|_n + \frac{\beta}{\beta + \tau}\omega_i^v|_{n-1}, \quad (45)$$

where, the subscripts $n-1$ and n denote two subsequent time/load steps, and $\Delta\tau$ is the interval between them, while τ is the time/load parameter.

It has been demonstrated that, when the viscosity parameter β is small compared to $\Delta\tau$, the viscous regularization scheme improves the rate of convergence without significantly affecting the accuracy of the results. Therefore, for all applications shown in the following section the value of $\beta = 1 \times 10^{-5}$ has been chosen.

4. Numerical validation and test results

In this section, some applications of the developed method are presented. The first test shows the spurious effects that may arise with the localization phenomena using a single-domain Ritz approach. Using a multi-domain discretization it is possible to obtain a meaningful response without un-physical behaviour. In all tests, the same order of polynomial for both directions was chosen, namely $M_\chi = N_\chi = p$.

4.1. Treatment of damage Gibbs artefacts

To illustrate the issues arising when coupling the single domain Ritz method with a localized damage representation, a square unidirectional composite lamina subjected to uniaxial tension is considered, as shown in Fig. 6. Moreover, a narrow band of material along the x_2 axis in the left vertical edge has strength lower than the rest of the plate, to artificially induce the onset of the damage. The plate has sides $L = H = 10$ mm, and the material properties are given in Table 1.

The analysis is performed in displacement control, by setting the maximum displacement $u_1 = 0.15$ mm. Fig. 7 shows the damage plot related to the damage index ω_{ft} in the fibre direction for different
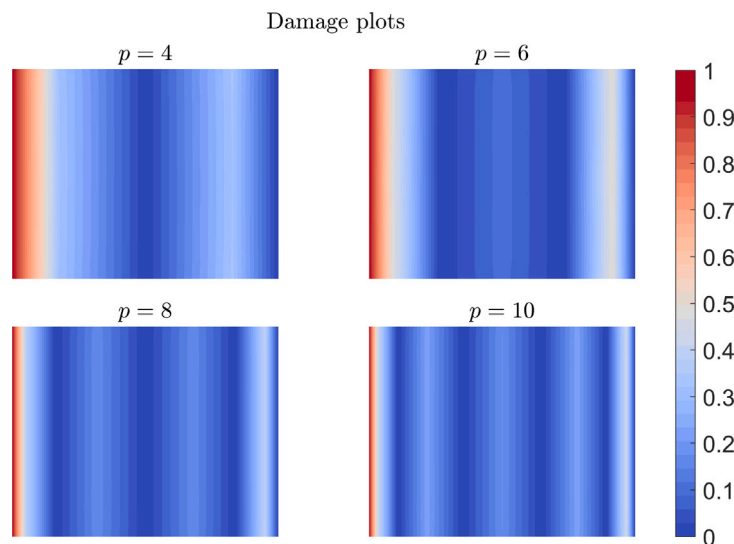

Fig. 7. Damage plot of ω_{ft} index for lamina in tension showing Gibbs effects.
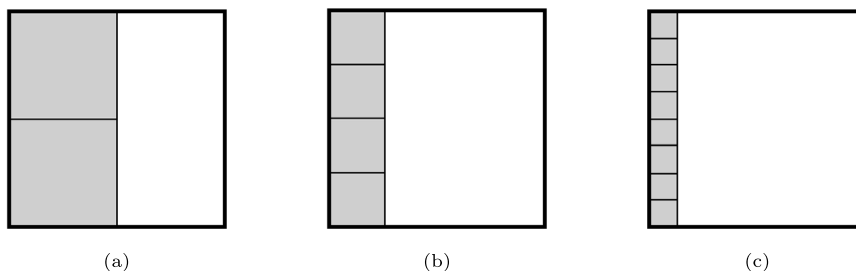
Fig. 8. Multi-domain discretizations used: (a) discretization 3E2B; (b) discretization 5E4B; (c) discretization 9E8B.
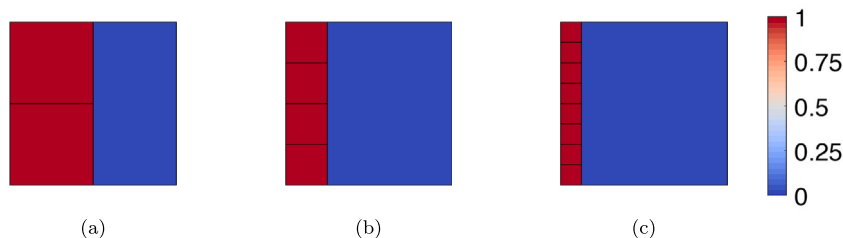

Fig. 9. Damage plots of ω_{f_t} index for lamina in tension adopting different discretizations showing the removal of Gibbs effect.
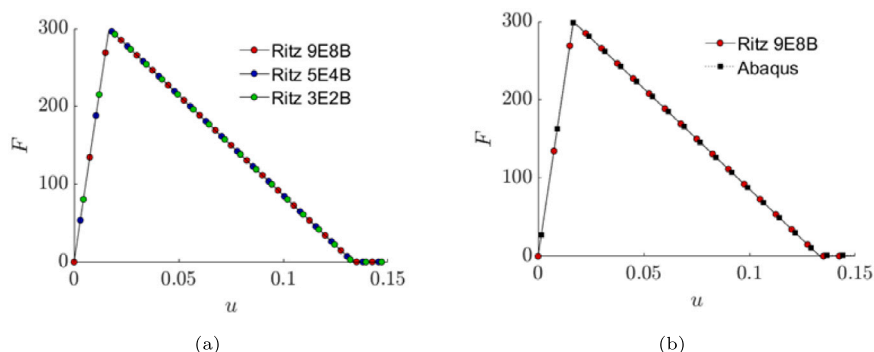

Fig. 10. Force-vs-displacement result of unidirectional composite lamina in tension: (a) comparison for three different discretizations showing discretization-independent results; (b) comparison of present method with ABAQUS.

polynomial expansions used in the Ritz approximation scheme. It is clear that the Gibbs effect is present and generates an oscillatory behaviour of the damage along the x_1 axis. The presence of Gibbs effects is due to the employment of the single domain Ritz method, which has a global support, for capturing a localized damage phenomenon. After reaching the peak stress, material points unaffected by damage generally unload. As a result, the strain values in contiguous material points can exhibit steep variations. Hence, the polynomial Ritz approximation in Eq. (31) may fail to capture such localized variation, giving rise to the mentioned Gibbs effect [57].

To address this inconvenience, this study has explored various methods, such as utilizing filters to minimize the presence of Gibbs ripples. Although such approaches have demonstrated some advantages, they were not able to fully remove Gibbs artefacts. Therefore, a strategy based on the adaptive multi-domain subdivision of the analysis domain has been considered. The same test as that performed above is now analysed using the adaptive multi-domain procedure schematically represented in the block diagram in Fig. 5. Starting from a single domain representation, the damage onset is triggered at the level of displacement $u_2 = 0.0165$ mm. At this stage, the multi-domain discretization procedure is activated. The new sub-domains, which are coloured in grey in Fig. 8, adopt a Ritz polynomial expansion of order $p = 1$, whilst the bigger sub-domain maintains a higher polynomial order, namely

$p = 4$, to retain a high level of accuracy. As shown in Fig. 8, three different discretizations were employed to verify the independence of the response from the number and the dimension of the sub-domains: (*i*) discretization of Fig. 8(a) is named *3E2B* and uses two sub-domains in the damaged band; (*ii*) discretization of Fig. 8(b) is named *5E4B* and uses four sub-domains in the damaged band; (*iii*) discretization of Fig. 8(c) is named *9E8B* and uses eighth sub-domains in the damaged band.

Damage plots related to each discretization used are reported in Fig. 9, where it appears that the Gibbs effect is completely removed.

Fig. 10(a) shows the result in terms of force-vs.-displacement, which confirms the independence of the type of multi-domain discretization used, thus validating the objectivity of the response. Finally, the solution of the present method is compared with FE results obtained with the ABAQUS built-in CDM model in Fig. 10(b). The comparison of the results shows excellent agreement with established FE analysis methods.

4.2. Method validation

For validation purposes and to assess the capabilities of the developed adaptive multi-domain Ritz method, another test is herein reported. The damage evolution in a composite unidirectional lamina
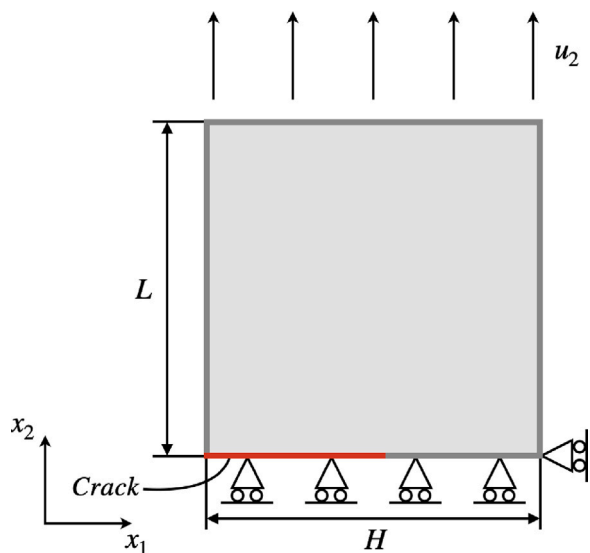
Fig. 11. Geometry and boundary condition for unidirectional lamina with a pre-existing crack.

Table 2
Properties of AS4/PEEK composite lamina.

Properties	Values
Modulus [GPa]	$E_{11} = 127.6$; $E_{22} = 10.8$; $G_{12} = G_{13} = 6.0$; $G_{23} = 5.7$
Poisson's ratio	$\nu_{12} = 0.32$
Strength [MPa]	$X^T = 2023.4$; $X^C = 1234.1$; $Y^T = 92.7$; $Y^C = 176.0$; $S^L = S^T = 186.0$
Fracture toughness [kJ m^{-2}]	$G_{c,ft} = 201$; $G_{c,fc} = 128$; $G_{c,mt} = 0.8$; $G_{c,mc} = 0.8$

under tensile load with a pre-existing crack spanning half length of the edge has been considered. The plate was modelled taking advantage of the symmetry to reduce the number of degrees of freedom. The geometry and boundary conditions of this test case are reported in Fig. 11. The half specimen modelled is a square plate with sides $L = H = 200$ mm and thickness $h = 1$ mm. Material properties for the composite material used are reported in Table 1 and the lamina has a fibre orientation $\theta = 0°$ with respect to the x_1 axis.

The whole plate domain was initially divided into three sub-domains as shown in Fig. 12(a), where the sub-domain (1) was used to model the pre-existing crack by setting all the damage indices $\omega_i = 1$.

During the incremental loading procedure, the damage starts developing at the crack tip. Hence, the adaptive refinement is activated following the procedure illustrated in Fig. 5. The damage propagates along the x_1 direction and the new sub-domains were added only next to the crack tip. Fig. 12(b) shows an intermediate discretization step where the subdomains in which the damage spread are coloured in grey. The final stage of discretization is reported in Fig. 12(c), where the damage is fully propagated along the side of the plate.

The solution convergence concerning the polynomial order has been evaluated by examining the total reaction force and displacement in the x_2 direction, as shown in Fig. 13(a). The analysis demonstrates that, in the specific case studied, rapid convergence is attained by utilizing a polynomial order of $p = 6$ for the undamaged sub-domains. These findings have been compared to results obtained using ABAQUS, employing a converged mesh composed of 20×20 finite elements. Fig. 13(b) illustrates a strong agreement between the results, validating the proposed approach. Furthermore, a reduction of approximately 60% in the number of degrees of freedom (DOFs) of the system can be observed: the proposed model, employing a polynomial expansion of $p = 6$, has a total of 1068 DOFs, while the FE analysis involves 2646 DOFs.

4.3. Notched VAT thermoplastic lamina

Subsequent tests were performed to show the behaviour of a single-edge notched VAT lamina loaded in tension. The schematic representation of the problem is reported in Fig. 11 with geometrical parameters $L = 1$ mm and $H = 0.75$ mm. The properties of the material used refer to an AS4/PEEK thermoplastic composite material that are reported in

Table 2. The analyses were performed in displacement control, using a maximum displacement increment $\Delta = 1 \times 10^{-4}$ mm which can be automatically adjusted during the iteration to obtain a convergent solution in the Newton–Raphson numerical procedure.

Four different VAT laminae were analysed having a fibre variation angle of $[0+\langle 30|0 \rangle]$, $[0+\langle 45|0 \rangle]$, $[0+\langle 0|30 \rangle]$ and $[0+\langle 0|45 \rangle]$ respectively. Fibre path representations for each lamina are reported in Fig. 14.

Fig. 15 shows the response in terms of force vs. displacements for the analysed laminae. For all configurations, after the linear-elastic branch, a nonlinear response occurs due to the onset and evolution of damage, up to the point where the lamina is completely broken.

The discretization employed at the beginning of the analysis was composed of three subdomains utilizing a polynomial order of $p = 12$ for each of them giving a total number of 3042 DOFs. In the final stage, the adaptive discretization results in a total number of 138 subdomains: 135 of order $p = 1$ were used to track the damage evolution, whilst 3 of order $p = 12$ were used for the undamaged subdomains, giving a total number of 6282 DOFs.

5. Discussion

In this section, some remarks about the potential, limitations and future developments of the method are discussed.

The proposed formulation offers valuable insights into the initiation, evolution, and failure of composite laminates, including VAT configurations, with a remarkable reduction in computational costs, in terms of number of DOFs with respect to more popular approaches. The developed tool may be used to efficiently investigate damage characteristics of VAT and classical laminates and find trade-off design solutions. However, it has been shown that the coupling of a classical single-domain Ritz approach, may result in an un-physical response, due to the spreading of spurious numerical effects. Hence, designers and engineers must consider the constraints and limitations associated with different modelling and computational tools while predicting the structural behaviour of composite materials and components.

The proposed adaptive hp-Ritz approach has shown to be a good alternative to classical FE-based analysis. It is worth noting that, the generalized displacements over the patches where damage localizes are approximated using first-order polynomials, whilst the larger undamaged sub-domains retain a higher polynomial degree to avoid losing accuracy. The use of first-order polynomials is crucial for representing uniform strain states in the damaged areas, which allows capturing uniform damage evolution within the considered damaged patches.

Although the proposed hp refinement solves the spurious effects arising in single domain approaches, classical CDM approaches still bear known issues linked with the discretization grids [50]. Indeed, the proposed technique can capture cases in which damage localizes in narrow bands while a single-domain approach succeeds in capturing cases where damage is distributed over a well-definite finite region [25]. In the last case, the introduction of a multi-domain splitting may incur in localization issues and associated spurious dependencies, analogously to what happens in FE-CDM models, if no regularization technique
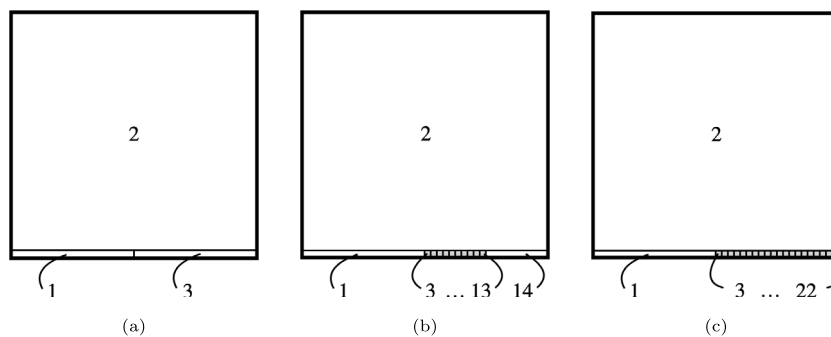
Fig. 12. Different phases of adaptive discretization used: (a) initial discretization; (b) intermediate discretization; (c) final discretization.
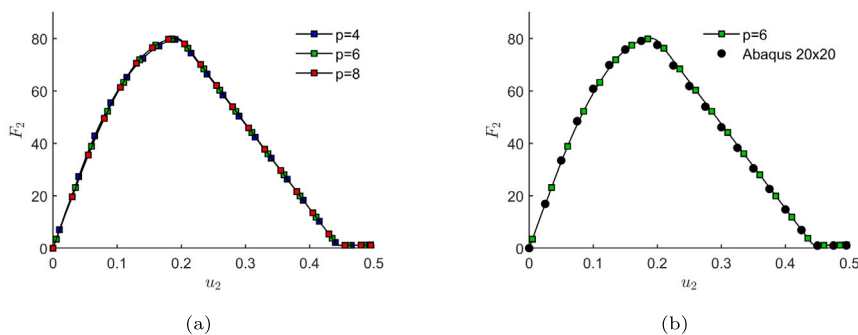

Fig. 13. Results of the composite lamina with pre-existing crack loaded in tension: (a) convergence analysis; (b) comparison of results with ABAQUS.
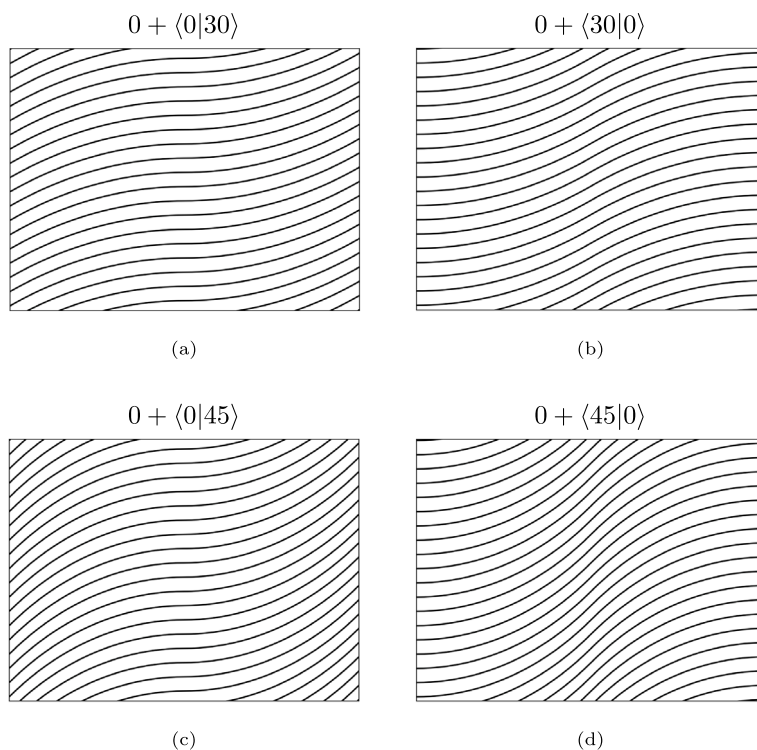

Fig. 14. Fibre path representations for each lamina analysed.

is adopted. Therefore, different damage models could be investigated, e.g. non-local, phase field or gradient approaches [48,58,59].

From a more physical standpoint, the model might be expanded to take into account additional damage mechanisms, such as impact-induced damage or inter-laminar delamination. Layer-wise displacement approximations along the thickness, hybrid variational statements [60], and cohesive inter-laminar traction–separation laws [61, 62] could all be used to describe delamination. The direct modelling of
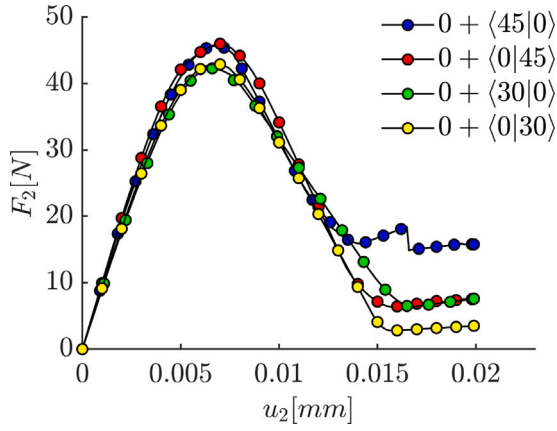
Fig. 15. Force vs. displacement curves for VAT AS4/PEEK thermoplastic composite laminae.

the displacement jump between adjacent layers and their relationship to inter-laminar damage, all the way to complete decohesion, would be made possible by these techniques. In order to trace the evolution of impact-induced damage, it is possible to examine contact mechanics laws that are appropriate for describing the localized mechanical effects of impacts [9] in conjunction with the incremental approach proposed in this work. Moreover, the present model can be extended to account for large strains. This can be done following the approach adopted for example in Refs. [19,20,25], where proper non-linear strain–displacement relationships are assumed and the suitable tangent stiffness matrix operator, considering both material and geometric non-linearities, is accordingly computed.

6. Conclusions

A non-linear Ritz methodology for the analysis of damage initiation and evolution up to failure in VAT composite plates under progressive loading has been developed, implemented and tested. The approach is based on first order shear deformation kinematics, the formulation of the equilibrium equations through energy minimization and the constitutive description of irreversible damage accumulation within the framework of continuum damage mechanics. The study has highlighted how the application of the method in a single-domain version generally incurs in the emergence of artefacts induced by the inability of polynomials with global support to represent localized phenomena, such as damage. The issue has been circumvented by developing an adaptive multi-domain Ritz approach, which still retains the advantages of Ritz formulation, namely a reduced number of degrees of freedom with respect to full field finite element analyses, and it is able to capture damage evolution, thus going beyond available Ritz formulation including damage in the form of an on/off parameter. The method has been assessed and validated through benchmark test cases and eventually some original results involving VAT composite plates have been presented, as future reference. Few directions for further investigation have been eventually identified and discussed.

CRediT authorship contribution statement

Dario Campagna: Conceptualization, Formal analysis, Investigation, Methodology, Software, Validation, Visualization, Writing – original draft. **Vincenzo Oliveri:** Conceptualization, Formal analysis, Investigation, Methodology, Software, Supervision, Writing – review & editing. **Ivano Benedetti:** Conceptualization, Formal analysis, Funding acquisition, Methodology, Project administration, Supervision, Writing – review & editing.

Data availability

Data will be made available on request.

Appendix A. Differential operator

The matrix linear differential operators appearing in Eq. (8b) are defined as

$$\boldsymbol{D}_p = \begin{bmatrix} \partial_{x_1} & 0 & 0 \\ 0 & \partial_{x_2} & 0 \\ \partial_{x_2} & \partial_{x_1} & 0 \end{bmatrix} \qquad \boldsymbol{D}_n = \begin{bmatrix} 0 & 0 & \partial_{x_1} \\ 0 & 0 & \partial_{x_2} \\ 0 & 0 & 0 \end{bmatrix} \qquad \text{(A.1)}$$

with $\partial_{x_i} = \partial(\circ)/\partial x_i$.

After combining Eqs. (2) and (A.1), the matrix elements of the differential operators becomes,

$$\partial_{x_1} = \frac{1}{J_{11}J_{22} - J_{12}J_{21}} \left(J_{22}\frac{\partial}{\partial \xi} - J_{12}\frac{\partial}{\partial \eta} \right) \qquad \text{(A.2a)}$$

$$\partial_{x_2} = \frac{1}{J_{11}J_{22} - J_{12}J_{21}} \left(-J_{21}\frac{\partial}{\partial \xi} + J_{11}\frac{\partial}{\partial \eta} \right) \qquad \text{(A.2b)}$$

where J_{ij} are the elements of the Jacobian matrix associated with the coordinate transformation.

Appendix B. Elastic matrices

Elastic coefficient matrices $\boldsymbol{Q}_p$ and $\boldsymbol{Q}_n$ appearing in Eq. (9) take the form,

$$\boldsymbol{Q}_p = \begin{bmatrix} Q_{11} & Q_{12} & Q_{16} \\ Q_{12} & Q_{22} & Q_{26} \\ Q_{16} & Q_{26} & Q_{66} \end{bmatrix} \qquad \boldsymbol{Q}_n = \begin{bmatrix} Q_{44} & Q_{45} & 0 \\ Q_{45} & Q_{55} & 0 \\ 0 & 0 & 0 \end{bmatrix} \qquad \text{(B.1)}$$

where,

$$Q_{11} = \hat{Q}_{11}\cos^4\theta + 2\left(\hat{Q}_{12} + 2\hat{Q}_{66}\right)\sin^2\theta\cos^2\theta + \hat{Q}_{22}\sin^4\theta \qquad \text{(B.2a)}$$

$$Q_{12} = \hat{Q}_{12}\cos^4\theta + \left(\hat{Q}_{11} + \hat{Q}_{22} - 4\hat{Q}_{66}\right)\sin^2\theta\cos^2\theta + \hat{Q}_{12}\sin^4\theta \qquad \text{(B.2b)}$$

$$Q_{22} = \hat{Q}_{11}\sin^4\theta + 2\left(\hat{Q}_{12} + 2\hat{Q}_{66}\right)\sin^2\theta\cos^2\theta + \hat{Q}_{22}\cos^4\theta \qquad \text{(B.2c)}$$

$$Q_{16} = \left(\hat{Q}_{11} - \hat{Q}_{12} - 2\hat{Q}_{66}\right)\sin\theta\cos^3\theta + \left(\hat{Q}_{12} - \hat{Q}_{22} + 2\hat{Q}_{66}\right)\sin^3\theta\cos\theta \qquad \text{(B.2d)}$$

$$Q_{26} = \left(\hat{Q}_{11} - \hat{Q}_{12} - 2\hat{Q}_{66}\right)\sin^3\theta\cos\theta + \left(\hat{Q}_{12} - \hat{Q}_{22} + 2\hat{Q}_{66}\right)\sin\theta\cos^3\theta \qquad \text{(B.2e)}$$

$$Q_{66} = \left(\hat{Q}_{11} + \hat{Q}_{22} - 2\hat{Q}_{12} - 2\hat{Q}_{66}\right)\sin^2\theta\cos^2\theta + \hat{Q}_{66}\left(\sin^6\theta\cos^4\theta\right)\cos\theta \qquad \text{(B.2f)}$$

$$Q_{44} = \hat{Q}_{44}\cos^2\theta + \hat{Q}_{55}\sin^2\theta \qquad \text{(B.2g)}$$

$$Q_{45} = \left(\hat{Q}_{55} - \hat{Q}_{44} \right) \cos \theta \sin \theta \tag{B.2h}$$

$$Q_{55} = \hat{Q}_{44} \sin^2 \theta + \hat{Q}_{55} \cos^2 \theta \tag{B.2i}$$

The stiffness coefficients in the material reference system $\hat{Q}_{ij}$ are collected in the matrices

$$\hat{Q}_p = \begin{bmatrix} \hat{Q}_{11} & \hat{Q}_{12} & 0 \\ \hat{Q}_{12} & \hat{Q}_{22} & 0 \\ 0 & 0 & \hat{Q}_{66} \end{bmatrix} \qquad \hat{Q}_n = \begin{bmatrix} \hat{Q}_{44} & 0 & 0 \\ 0 & \hat{Q}_{55} & 0 \\ 0 & 0 & 0 \end{bmatrix} \tag{B.3}$$

being,

$$\hat{Q}_{11} = \frac{E_1}{1 - \nu_{12}\nu_{21}} \qquad \hat{Q}_{22} = \frac{E_2}{1 - \nu_{12}\nu_{21}} \qquad \hat{Q}_{12} = \frac{\nu_{12}E_2}{1 - \nu_{12}\nu_{21}} \tag{B.4a}$$

$$\hat{Q}_{66} = G_{12} \qquad \hat{Q}_{44} = G_{23} \qquad \hat{Q}_{55} = G_{13} \tag{B.4b}$$

where E_i are the Young's moduli, G_{ij} are the shear moduli and ν_{ij} are the Poisson's coefficients respectively.

Appendix C. Resolving system matrices

Matrices appearing in Eq. (35) have the following expressions

$$K_0 = \int_{\Omega} \begin{bmatrix} \left(B_{pU}^{\mathsf{T}} A B_{pU} + B_{nU}^{\mathsf{T}} A_s B_{nU} \right) & \left(B_{pU}^{\mathsf{T}} B B_{p\Theta} + B_{nU} A_s B_{i\Theta} \right) \\ \left(B_{p\Theta}^{\mathsf{T}} B B_{pU} + B_{i\Theta}^{\mathsf{T}} A_s B_{nU} \right) & \left(B_{p\Theta}^{\mathsf{T}} D B_{p\Theta} + B_{i\Theta} A_s B_{i\Theta} \right) \end{bmatrix} d\Omega,$$

$$R = \int_{\Omega} \begin{bmatrix} \Phi_u^{\mathsf{T}} \Xi_u^{\mathsf{T}} \mu_u \Xi_u \Phi_u & 0 \\ 0 & \Phi_\vartheta^{\mathsf{T}} \Xi_\vartheta^{\mathsf{T}} \mu_\vartheta \Xi_\vartheta \Phi_\vartheta \end{bmatrix} d\Omega,$$

$$F_L = \int_{\Omega} \left\{ \begin{matrix} \Phi_u^{\mathsf{T}} q \\ \Phi_\vartheta^{\mathsf{T}} m \end{matrix} \right\} d\Omega + \int_{\partial\Omega_l} \left\{ \begin{matrix} \Phi_u^{\mathsf{T}} \overline{N} \\ \Phi_\vartheta^{\mathsf{T}} \overline{M} \end{matrix} \right\} d\partial\Omega,$$

$$F_D = \int_{\partial\Omega_c} \left\{ \begin{matrix} \Phi_u^{\mathsf{T}} \Xi_u^{\mathsf{T}} \mu_u \Xi_u \bar{u} \\ \Phi_\vartheta^{\mathsf{T}} \Xi_\vartheta^{\mathsf{T}} \mu_\vartheta \Xi_\vartheta \bar{\vartheta} \end{matrix} \right\} d\partial\Omega. \tag{C.1}$$

The penalty matrix used for connection between subdomains appearing in Eq. (40) is given by

$$P_{pt}^{\langle r,s \rangle} = \int_{\Gamma_{pt}} \begin{bmatrix} \left(\Phi_u^{\langle r \rangle T} \Lambda_u^{\langle r \rangle T} \mu_u^{\langle pt \rangle} \Lambda_u^{\langle s \rangle} \Phi_u^{\langle s \rangle} \right) & 0 \\ 0 & \left(\Phi_\vartheta^{\langle r \rangle T} \Lambda_\vartheta^{\langle r \rangle T} \mu_\vartheta^{\langle pt \rangle} \Lambda_\vartheta^{\langle s \rangle} \Phi_\vartheta^{\langle s \rangle} \right) \end{bmatrix} d\Gamma \tag{C.2}$$

Appendix D. Tangent stiffness matrix contributions

The tangent stiffness matrix contribution $K_{t,dmg}$ is related to the damage evolution in Eq. (37). Regarding the first term, from Eq. (37) ones can write

$$\Delta \left(K_0 X \right) = K_0 \Delta X + \Delta K_0 X. \tag{D.1}$$

The second term of the right hand-side in Eq. (D.1) can be written as

$$\Delta K_0 X = \Delta \begin{bmatrix} K_0^{11} & K_0^{12} \\ K_0^{21} & K_0^{22} \end{bmatrix} \left\{ \begin{matrix} U \\ \Theta \end{matrix} \right\}. \tag{D.2}$$

The detailed computation is developed only for the first term K_0^{11} of the matrix appearing in Eq. (D.2), being the computation of the other terms similar. One may write

$$\Delta \left(K_0^{11} \right) U = \Delta \left[\int_{\Omega} \left(B_{pU}^{\mathsf{T}} A B_{pU} + B_{nU}^{\mathsf{T}} A_s B_{nU} \right) d\Omega \right] U \tag{D.3}$$

and then, noting that, in the present formulation, the second term within the integral sign does not depend on damage, recalling Eq. (34)

$$\Delta \left(K_0^{11} \right) U = \int_{\Omega} \sum_{i,k} \int_{h_{k-1}}^{h_k} B_{pU}^{\mathsf{T}} \Delta \left(Q_{p,i} \right) B_{pU} U dx_3 d\Omega =$$

$$= \int_{\Omega} \sum_{i,k} \int_{h_{k-1}}^{h_k} B_{pU}^{\mathsf{T}} \frac{\partial Q_{p,i}}{\partial \omega_i^v} \frac{\partial \omega_i^v}{\partial \omega_i} \frac{\partial \omega_i}{\partial e_{i,eq}} \frac{\partial e_{i,eq}}{\partial e_p} \frac{\partial e_p}{\partial X} \Delta X B_{pU} U dx_3 d\Omega \tag{D.4}$$

where the derivation chain rule has been applied and the summation is intended for $i \in \{ ft, fc, mt, mc \}$ and $k \in [1, N_{ply}]$. The derivatives involved in Eq. (D.4) may be computed as

$$\frac{\partial \omega_i^v}{\partial \omega_i} = \frac{\Delta \tau}{\beta + \Delta \tau}, \qquad \frac{\partial \omega_i}{\partial e_{i,eq}} = \frac{\alpha_i}{\alpha_i - 1} \left(\frac{e_{i,eq}^0}{e_{i,eq}^2} \right),$$

$$\frac{\partial e_{i,eq}}{\partial e_p} = \left\{ \frac{\partial e_{i,eq}}{\partial e_{11}} \quad \frac{\partial e_{i,eq}}{\partial e_{22}} \quad \frac{\partial e_{i,eq}}{\partial e_{12}}, \right\} \tag{D.5}$$

$$\frac{\partial e_p}{\partial X} \Delta X = B_{pU} \Delta U + x_3 B_{p\Theta} \Delta \Theta,$$

where

$$\alpha_i = \frac{2 G_{c,i}}{e_{eq}^0 \sigma_{eq}^0 L_c} \tag{D.6}$$

Noting that the product of Eqs. (D.5) results in a scalar, this block is conveniently moved at the end of the integral as follows

$$\int_{\Omega} \sum_{i,k} \int_{h_{k-1}}^{h_k} B_{pU}^{\mathsf{T}} \frac{\partial Q_{p,i}}{\partial \omega_i^v} B_{pU} U \frac{\partial \omega_i^v}{\partial \omega_i} \frac{\partial \omega_i}{\partial e_{i,eq}} \frac{\partial e_{i,eq}}{\partial e_p} \frac{\partial e_p}{\partial X} \Delta X dx_3 d\Omega$$

$$= \int_{\Omega} B_{pU}^{\mathsf{T}} \left[\sum_{i,k} \int_{h_{k-1}}^{h_k} \frac{\partial Q_{p,i}}{\partial \omega_i} B_{pU} U \zeta(\alpha_i, \beta, \Delta\tau) dx_3 \right] B_{pU} \Delta U$$

$$+ B_{pU}^{\mathsf{T}} \left[\sum_{i,k} \int_{h_{k-1}}^{h_k} \frac{\partial Q_{p,i}}{\partial \omega_i} B_{pU} U \zeta(\alpha_i, \beta, \Delta\tau) x_3 dx_3 \right] B_{pU} \Delta \Theta \tag{D.7}$$

$$= \int_{\Omega} B_{pU}^{\mathsf{T}} A^{*,1} B_{pU} \Delta U + B_{pU}^{\mathsf{T}} B^{*,1} B_{pU} \Delta \Theta d\Omega,$$

where

$$\zeta(\alpha_i, \beta, \Delta\tau) = \frac{\Delta \tau}{\beta + \Delta \tau} \frac{\alpha_i}{\alpha_i - 1} \left(\frac{e_{i,eq}^0}{e_{i,eq}^2} \right) \frac{\partial e_{i,eq}}{\partial e_p}. \tag{D.8}$$

Repeating the same procedures for all the elements of the matrix K_0, the final expression of the matrix $K_{t,dmg}$ is obtained as

$$K_{t,dmg} = K_0 + \int_{\Omega} \begin{bmatrix} B_{pU}^{\mathsf{T}} A^* B_{pU} & B_{pU}^{\mathsf{T}} B^* B_{p\Theta} \\ B_{p\Theta}^{\mathsf{T}} B^* B_{pU} & B_{p\Theta}^{\mathsf{T}} D^* B_{p\Theta} \end{bmatrix} d\Omega, \tag{D.9}$$

where

$$A^* = \sum_{i,k} \int_{h_{k-1}}^{h_k} \frac{\partial Q_{p,i}}{\partial \omega_i^i} \left(B_{pU} U + x_3 B_{p\Theta} \Theta \right) \zeta(\alpha_i, \beta, \Delta\tau) dx_3,$$

$$B^* = \sum_{i,k} \int_{h_{k-1}}^{h_k} \frac{\partial Q_{p,i}}{\partial \omega_i^i} \left(B_{pU} U + x_3 B_{p\Theta} \Theta \right) \zeta(\alpha_i, \beta, \Delta\tau) x_3 dx_3, \tag{D.10}$$

$$D^* = \sum_{i,k} \int_{h_{k-1}}^{h_k} \frac{\partial Q_{p,i}}{\partial \omega_i^i} \left(B_{pU} U + x_3 B_{p\Theta} \Theta \right) \zeta(\alpha_i, \beta, \Delta\tau) x_3^2 dx_3.$$

References

[1] Parandoush P, Lin D. A review on additive manufacturing of polymer-fiber composites. Compos Struct 2017;182:36–53.

[2] Yassin K, Hojjati M. Processing of thermoplastic matrix composites through automated fiber placement and tape laying methods: A review. J Thermoplast Compos Mater 2018;31(12):1676–725.

[3] Oliveri V, Zucco G, Peeters D, Clancy G, Telford R, Rouhi M, McHale C, O'Higgins RM, Young TM, Weaver PM. Design, manufacture and test of an in-situ consolidated thermoplastic variable-stiffness wingbox. AIAA J 2019;57(4):1671–83.

[4] Dhinakaran V, Surendar K, Hasunfur Riyaz M, Ravichandran M. Review on study of thermosetting and thermoplastic materials in the automated fiber placement process. Mater Today: Proc 2020;27:812–5, First International conference on Advanced Lightweight Materials and Structures.

[5] Gürdal Z, Tatting B, Wu C. Variable stiffness composite panels: Effects of stiffness variation on the in-plane and buckling response. Composites A 2008;39(5):911–22.

[6] Milazzo A, Oliveri V. Investigation of buckling characteristics of cracked variable stiffness composite plates by an extended Ritz approach. Thin-Walled Struct 2021;163:107750.

[7] Sciascia G, Oliveri V, Weaver PM. Dynamic analysis of prestressed variable stiffness composite shell structures. Thin-Walled Struct 2022;175:109193.

[8] Sciascia G, Oliveri V, Weaver PM. Dynamic performance of hygrothermal mechanically preloaded variable-stiffness composite fairing structures. AIAA J 2023;1–18.

[9] Milazzo A, Benedetti I. A non-linear ritz method for the analysis of low velocity impact induced dynamics in variable angle tow composite laminates. Compos Struct 2021;276.

[10] Kant T, Pandya B. A simple finite element formulation of a higher-order theory for unsymmetrically laminated composite plates. Compos Struct 1988;9(3):215–46.

[11] Carrera E. Theories and finite elements for multilayered, anisotropic, composite plates and shells. Arch Comput Methods Eng 2002;9(2):87–140.

[12] Demasi L. Treatment of stress variables in advanced multilayered plate elements based upon Reissner's mixed variational theorem. Comput Struct 2006;84(19):1215–21.

[13] Caliri Jr MF, Ferreira AJ, Tita V. A review on plate and shell theories for laminated and sandwich structures highlighting the finite element method. Compos Struct 2016;156:63–77.

[14] Demasi L, Biagini G, Vannucci F, Santarpia E, Cavallaro R. Equivalent single layer, zig-zag, and layer wise theories for variable angle tow composites based on the generalized unified formulation. Compos Struct 2017;177:54–79.

[15] Tornabene F, Fantuzzi N, Bacciocchi M. The GDQ method for the free vibration analysis of arbitrarily shaped laminated composite shells using a NURBS-based isogeometric approach. Compos Struct 2016;154:190–218.

[16] Gulizzi V, Benedetti I, Milazzo A. An implicit mesh discontinuous Galerkin formulation for higher-order plate theories. Mech Adv Mater Struct 2020;27(17):1494–508.

[17] Gulizzi V, Benedetti I, Milazzo A. A high-resolution layer-wise discontinuous Galerkin formulation for multilayered composite plates. Compos Struct 2020;242:112137.

[18] Benedetti I, Gulizzi V, Milazzo A. Layer-wise discontinuous Galerkin methods for piezoelectric laminates. Modelling 2020;1(2):198–214.

[19] Milazzo A, Oliveri V. Buckling and postbuckling of stiffened composite panels with cracks and delaminations by Ritz approach. AIAA J 2017;55(3):965–80.

[20] Oliveri V, Milazzo A. A Rayleigh-Ritz approach for postbuckling analysis of variable angle tow composite stiffened panels. Comput Struct 2018;196:263–76.

[21] Milazzo A, Benedetti I, Gulizzi V. An extended Ritz formulation for buckling and post-buckling analysis of cracked multilayered plates. Compos Struct 2018;201:980–94.

[22] Milazzo A, Benedetti I, Gulizzi V. A single-domain Ritz approach for buckling and post-buckling analysis of cracked plates. Int J Solids Struct 2019;159:221–31.

[23] Lopes C, Camanho P, Gürdal Z, Tatting B. Progressive failure analysis of tow-placed, variable-stiffness composite panels. Int J Solids Struct 2007;44(25):8493–516.

[24] Pan Z, Zhang L, Liew K. A phase-field framework for failure modeling of variable stiffness composite laminae. Comput Methods Appl Mech Engrg 2022;388:114192.

[25] Campagna D, Milazzo A, Benedetti I, Oliveri V. A non-linear Ritz method for progressive failure analysis of variable angle tow composite laminates. Mech Adv Mater Struct 2023;30(5):995–1008.

[26] González C, LLorca J. Mechanical behavior of unidirectional fiber-reinforced polymers under transverse compression: Microscopic mechanisms and modeling. Compos Sci Technol 2007;67(13):2795–806.

[27] Benedetti I, Gulizzi V, Milazzo A. A microstructural model for homogenisation and cracking of piezoelectric polycrystals. Comput Methods Appl Mech Engrg 2019;357:112595.

[28] Lo Cascio M, Milazzo A, Benedetti I. Coupled VEM–BEM approach for isotropic damage modelling in composite materials. J Multiscale Model 2023;14(01):2341001.

[29] Bergan A, Dávila C, Leone F, Awerbuch J, Tan T-M. A mode I cohesive law characterization procedure for through-the-thickness crack propagation in composite laminates. Composites B 2016;94:338–49.

[30] Li S, Thouless M, Waas A, Schroeder J, Zavattieri P. Use of a cohesive-zone model to analyze the fracture of a fiber-reinforced polymer–matrix composite. Compos Sci Technol 2005;65(3):537–49.

[31] Rudraraju SS, Salvi A, Garikipati K, Waas AM. In-plane fracture of laminated fiber reinforced composites with varying fracture resistance: Experimental observations and numerical crack propagation simulations. Int J Solids Struct 2010;47(7):901–11.

[32] Matzenmiller A, Lubliner J, Taylor RL. A constitutive model for anisotropic damage in fiber-composites. Mech Mater 1995;20(2):125–52.

[33] Ladeveze P, LeDantec E. Damage modelling of the elementary ply for laminated composites. Compos Sci Technol 1992;43(3):257–67.

[34] Lapczyk I, Hurtado JA. Progressive damage modeling in fiber-reinforced materials. Composites A 2007;38(11):2333–41.

[35] Maimí P, Camanho PP, Mayugo J, Dávila C. A continuum damage model for composite laminates: Part I–constitutive model. Mech Mater 2007;39(10):897–908.

[36] Maimí P, Camanho P, Mayugo J, Dávila C. A continuum damage model for composite laminates: Part II - computational implementation and validation. Mech Mater 2007;39:909–19.

[37] Ladeveze P, Allix O, Gornet L, Lévêque D, Perret L. A computational damage mechanics approach for laminates: identification and comparison with experimental results. In: Studies in applied mechanics, vol. 46, Elsevier; 1998, p. 481–500.

[38] Falzon B, Apruzzese P. Numerical analysis of intralaminar failure mechanisms in composite structures. Part I: FE implementation. Compos Struct 2011;93(2):1039–46.

[39] Falzon B, Apruzzese P. Numerical analysis of intralaminar failure mechanisms in composite structures. Part II: Applications. Compos Struct 2011;93(2):1047–53.

[40] Benedetti I, Nguyen H, Soler-Crespo RA, Gao W, Mao L, Ghasemi A, Wen J, Nguyen S, Espinosa HD. Formulation and validation of a reduced order model of 2D materials exhibiting a two-phase microstructure as applied to graphene oxide. J Mech Phys Solids 2018;112:66–88.

[41] Jirásek M, Desmorat R. Localization analysis of nonlocal models with damage-dependent nonlocal interaction. Int J Solids Struct 2019;174:1–17.

[42] Yang QJ, Hayman B. Simplified ultimate strength analysis of compressed composite plates with linear material degradation. Composites B 2015;69:13–21.

[43] Reddy JN. Mechanics of laminated composite plates and shells: theory and analysis. CRC Press; 2003.

[44] Jones RM. Mechanics of composite materials. CRC Press; 1993.

[45] Hashin Z, Rotem A. A fatigue failure criterion for fiber reinforced materials. J Compos Mater 1973;7(4):448–64.

[46] Hashin Z. Failure criteria for unidirectional fiber composites. J Appl Mech 1980;47(2):329–34.

[47] Bažant ZP, Oh BH. Crack band theory for fracture of concrete. Matér Constr 1983;16(3):155–77.

[48] Bažant ZP, Jirásek M. Nonlocal integral formulations of plasticity and damage: Survey of progress. J Eng Mech 2002;128(11):1119–49.

[49] Jirásek M, Bauer M. Numerical aspects of the crack band approach. Comput Struct 2012;110–111:60–78.

[50] Lopes B, Arruda M, Almeida-Fernandes L, Castro L, Silvestre N, Correia J. Assessment of mesh dependency in the numerical simulation of compact tension tests for orthotropic materials. Compos C 2020;1:100006.

[51] Smith ST, Bradford MA, Oehlers DJ. Numerical convergence of simple and orthogonal polynomials for the unilateral plate buckling problem using the Rayleigh–Ritz method. Internat J Numer Methods Engrg 1999;44:1685–707.

[52] Zienkiewicz OC, Taylor RL. The finite element method: solid mechanics. Vol. 2, Butterworth-heinemann; 2000.

[53] Reddy JN. Energy principles and variational methods in applied mechanics. John Wiley & Sons; 2017.

[54] MATLAB. 9.10.0.1710957 (R2021a) update 4. Natick, Massachusetts: The MathWorks Inc.; 2021.

[55] Maimí P, Camanho PP, Mayugo J-A, Dávila CG. A thermodynamically consistent damage model for advanced composites. Tech. rep. TM-2006-214282, NASA; 2006.

[56] Björck Å. Numerical methods for least squares problems. SIAM; 1996.

[57] Davis JM, Hagelstein P. Gibbs phenomena for some classical orthogonal polynomials. J Math Anal Appl 2022;505(1):125574.

[58] de Borst R, Verhoosel CV. Gradient damage vs phase-field approaches for fracture: Similarities and differences. Comput Methods Appl Mech Engrg 2016;312:78–94.

[59] Natarajan S, Annabattula RK, et al. Modeling crack propagation in variable stiffness composite laminates using the phase field method. Compos Struct 2019;209:424–33.

[60] Benedetti I, Milazzo A. Advanced models for smart multilayered plates based on Reissner mixed variational theorem. Composites B 2017;119:215–29.

[61] Benedetti I, Aliabadi M. A three-dimensional cohesive-frictional grain-boundary micromechanical model for intergranular degradation and failure in polycrystalline materials. Comput Methods Appl Mech Engrg 2013;265:36–62.

[62] Parrinello F, Benedetti I. A coupled plasticity-damage cohesive-frictional interface for low-cycle fatigue analysis. Int J Mech Sci 2022;224:107298.